Precise Free-Induction-Decay Magnetometry Using Cs MEMS Cells

A. McWilliam*, D. Hunter, J. P. McGilligan, T. Dyer, P. F. Griffin and E. Riis
Department of Physics, SUPA
University of Strathclyde, 107 Rottenrow East, Glasgow
UNITED KINGDOM

allan.mcwilliam@strath.ac.uk

ABSTRACT

In this work we explore the construction and the sensitivity of an optically pumped magnetometer operating in a free-induction-decay mode. We implement a co-propagating dual-laser system in this configuration to create a net spin polarisation through optical pumping in microfabricated Cs MEMS vapour cells. The effect of the optical pumping light can be tailored and enhanced for magnetic field strengths close to that of the Earth's by employing synchronous amplitude modulation. The obtained signals displaying the free-induction-decay (free-spin-precession) of the Cs atoms are presented and analysed. The key steps of effectively spin-polarising the Cs atoms and utilising cells with greater thicknesses, to obtain higher SNRs and sensitivities in the $fT/\sqrt{Hz}$ levels are presented.

1.0 INTRODUCTION

The importance of obtaining precise magnetic field measurements is crucial in several areas of scientific research and applications including archaeology [1], geophysical surveying [2] and for revealing undetonated ordinance [3]. Additionally, continuous research has revealed promising applications within the medical field such as in magnetocardiography (MCG) [4] and magnetoencephalography (MEG) [5]. Traditionally, the most sensitive measurements were provided using superconducting quantum interference devices (SQUIDs) which spearheaded the industry. These were particularly useful for MEG purposes, however, their bulkiness and operational need for cryogenic cooling is an impediment.

Optically pumped magnetometers (OPMs), a more practical type of magnetic sensor that monitors the behaviour of alkali-metal atoms after interacting with resonant laser light now have a firm foothold in the industry [6]. By directly measuring the precession frequency of a spin polarised atomic ensemble they provide extremely accurate magnetic field measurements. The most sensitive magnetic field sensor developed to date is the spin exchange relaxation free (SERF) sensor, which operates at near-zero magnetic fields within shielded enclosures. As published in [7], an impressive sensitivity of 160 $aT/\sqrt{Hz}$ has already been demonstrated in the SERF regime. However, these sensors do not easily lend themselves towards unshielded magnetic sensing applications. For unshielded, and real-world sensing applications a total field sensor such as the free-induction-decay (FID) magnetometer is more appropriate as they have the dynamic range required to operate in Earth's field conditions [8].

FID schemes are quite simple to implement and can be operated without a need for additional oscillating RF fields used in other types of OPM schemes [9]. The FID approach also presents an advantage in accuracy over setups with driven feedback schemes which can be affected by systematic errors during the readout [10]. The fully optical nature also circumvents the issue of crosstalk between networks of adjacent sensors which are necessary for MEG applications. An advancement for this application was made recently by operating a FID magnetometer in a gradiometric setup within the Earth's magnetic field [11]. A gradiometric noise floor of 16 $fT/cm/\sqrt{Hz}$ was reported and the research confirms a real progression for prospective usage of OPMs in MEG network arrays. Other works have employed FID in a gradiometer mode in a multi-beam-pass configuration to produce a sensitivity close to 10 $fT/cm/\sqrt{Hz}$ [12], further solidifying its promise for use in unshielded environments.

In this work we propose a scheme where two independent co-propagating beams are utilised in an FID configuration in a similar vein to the work in [13]. The experimental setup is used to generate FID signals in two Cs MEMS (micro-electro-mechanical systems) vapour cells of different thicknesses. Optical pumping using synchronous amplitude modulation (AM) with circularly polarised light is used to create an atomic orientation in each cell. A linearly polarised probe laser is then used to detect the Faraday rotation of the spin-polarised atoms around a transversely applied magnetic field. We compare the results obtained from these cells through improved spin-polarisation at Earth's magnetic field strength (approx. 50 µT).

2.0 FID MAGNETOMETRY

Fundamentally OPMs including the FID sensor operate by measuring the Larmor precession frequency of polarised atomic spins around an external magnetic field [6]. Polarisation of the atoms is induced through optical pumping, after which a torque on the atoms exerted by the magnetic field causes said precession. Through employing a linearly polarised probe beam, a measurement of this Larmor precession facilitates a calculation of the magnetic field strength via the simple relation $\omega_L = \gamma \vec{B}$, where γ is the gyromagnetic ratio, representing the ratio of a particles magnetic moment to its angular momentum. For the ground state of Cs, the value is fixed at around 3.5 Hz/nT [14]. An illustration of an OPM's fundamental process is shown in Figure 1.
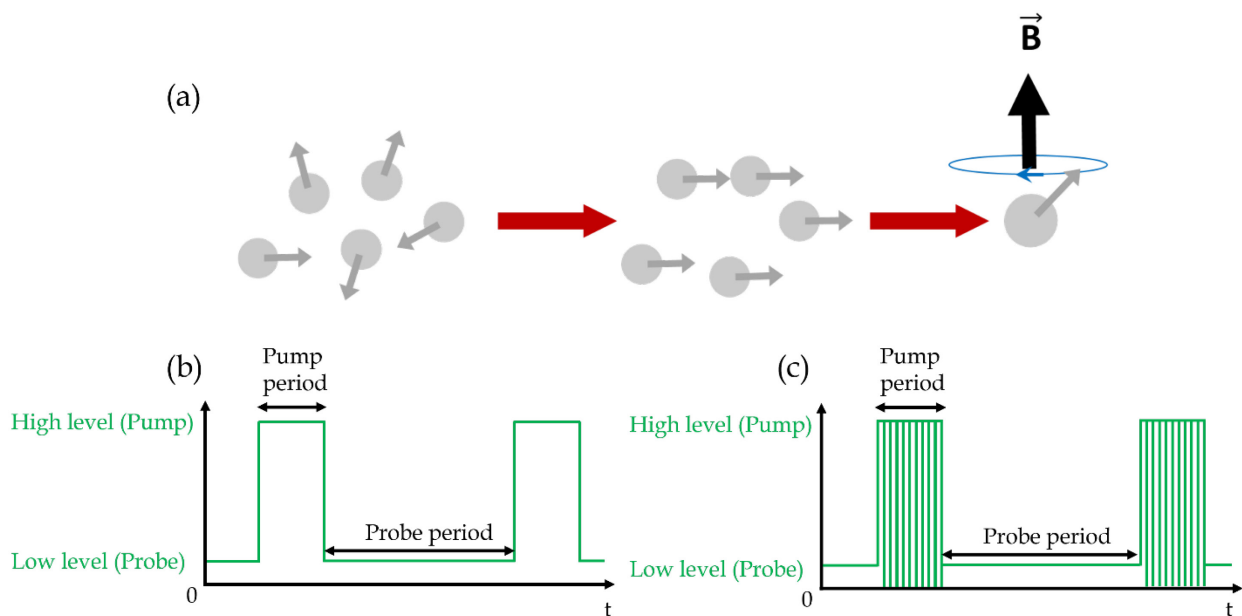

Figure 1: In the FID configuration an initially unpolarised ensemble of Cs atoms are polarised via interaction with resonant laser light through optical pumping. The free spin precession of these atoms around a transverse static magnetic field $\vec{B}$ can be observed and measured. Two separate regimes where the optical pumping light is amplitude modulated through a single pulse of light or synchronously at the Larmor frequency is illustrated in (b) and (c) respectively.

The FID technique is well known throughout other areas of science including nuclear magnetic resonance (NMR), where nuclear spins are polarised in a similar fashion to that of the optically active electrons in this work [15]. In FID systems, optical pumping is typically performed using a pulsed approach with the pumping and probing confined to two separate stages in the time domain [13]. The basic principle is to create a high net polarisation in the atomic ensemble through strong optical pumping and then to switch off the optical pumping light and monitor the free-induction-decay with either an independent or a less intense

probe laser. Specifically for this work, circularly polarised pump light is used to generate an atomic orientation in the sample, through the manipulation of populations in the Zeeman sublevels of the Cs hyperfine ground state [16]. This population disproportion into a specific Zeeman level can be pictured macroscopically through a classical model of a net magnetisation vector being orientated in the direction of beam propagation.

Notably, FID magnetometry enables an unambiguous reading of the magnetic field as the free spin precession of the polarised atoms is directly observed [8]. The signal has the form of a decaying sinusoid and is typically detected via a polarimeter connected to an oscilloscope or other DAQ device. The following nonlinear equation, which models a damped sinusoidal function is used to extract the experimental parameters.

$$S_n = A \sin(\omega_L n + \varphi_0) e^{-\gamma_2 n} + \epsilon_n$$

Modelling the FID data with this equation provides important information including the amplitude, which provides an indicator of the polarisation and magnetisation vector built up during the pump stage. From the decay rate we obtain information on the atomic coherence lifetimes, an important value which limits the potential sensitivity of the device. Maintaining the spin coherence in the sample is crucial for prolonging the measurement time and for the sensitivity of the sensor. Depolarising mechanisms from several contributions can occur, including spin destruction from collisions with the cell walls and from spin exchange collisions [17]. For the MEMS cells used in this work spin exchange is the primary depolarisation contribution. For this type of magnetometer, however, there remains a potential route towards suppression of spin exchange depolarisation. More efficiently optical pumping the atoms should distribute more Cs atoms into the stretched Zeeman state. This remains an encouraging route towards the suppression of spin exchange collisions, through a phenomenon known as light narrowing [18]. Critically, this spin exchange suppression actively reduces the decay rate and in turn, increases the atomic coherence lifetime.

The optical pumping efficiency can also be improved through AM to the pump laser light. For lower magnetic field strengths of around a few µT a single pulse of light can be effective in polarising the ensemble before the signal is read out during the probe stage. For higher magnetic field strengths (on the order of tens of µT and above), synchronous modulation is more favourable. This is a result of the total pump time limiting the total Larmor oscillations in the synchronous regime at lower fields due to the lower precession frequency. Conversely, at higher fields, single pulse AM tends to become inefficient due to the depolarisation caused by the higher precession frequency around the transverse field. These respective modulation techniques are depicted in (b) and (c) of Figure 1. The commonality between these regimes is to employ a higher laser intensity during the optical pumping stage and then to reduce the laser power to a lower level once the pump period is over for the probing stage. The lower power during the readout stage is vital to not further perturb or depolarise the atoms toward the direction of beam propagation, as the phase coherence from those freely precessing around the field would be eradicated. The major difference for the synchronous regime is that the Larmor precession is enhanced by modulating the light intensity at the Larmor frequency during the pumping stage.

3.0 EXPERIMENTAL SETUP

The key advancement to the FID experiment from previous works is the introduction of an additional laser source [8]. This should lead to improved signals as the pumping and probing stages are now decoupled. The MEMS vapour cell serves as the magnetic sensor and is placed within an oven inside a three-layer mu-metal shield, which suppresses the surrounding magnetic field and magnetic noise contributions from external sources. A resistive heater wire is wrapped around the oven and a current is delivered in order to heat the cell. The heater is switched off during the measurements to prevent any additional magnetic field distortion. Raising the temperature of the cell is critical in raising the atomic vapour density leading to a greater light-

atom interaction and thus signal-to-noise ratio (SNR). Counteracting the positive impact of raising the cell temperature is the increased decoherence rate which occurs at higher temperatures, therefore a balance between these is needed. For the MEMS vapour cells used in this experiment the ideal temperature is around 80 ℃.

Surrounding the cell are two sets of Helmholtz coils which can provide the static magnetic field control and orientation along the z and x directions. The static field is applied from only one set of Helmholtz coils orientated in the z direction, which is transverse to the direction of beam propagation. Figure 2 illustrates a simplified schematic of the dual-beam FID magnetometry setup.
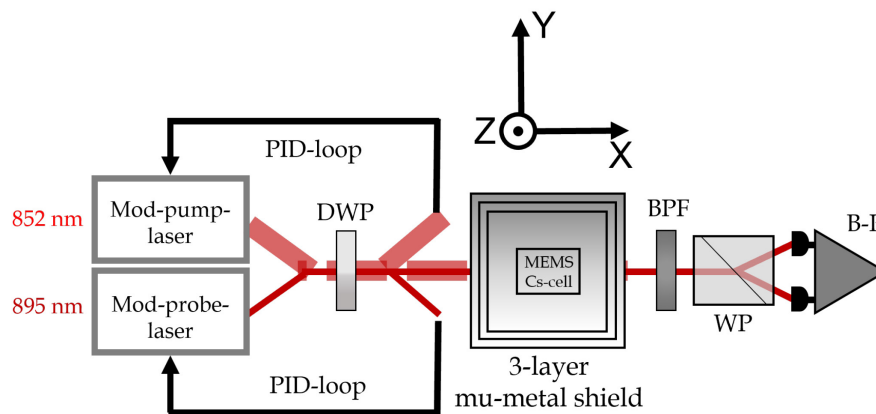

Figure 2: FID magnetometry setup. A dual laser system is used with independent pump and probe control. The laser beams are collinear and interact with the Cs vapour cell within a three-layer mu-metal shield. A set of Helmholtz coils is used to produce a bias magnetic field of 50 µT along the z direction. A band-pass filter blocks the 852 nm pump light and allows the 895 nm probe light to be directed towards the polarimeter for detection. (DWP, dual wavelength wave plate; BPF, band pass filter; WP, Wollaston prism; B-P, balanced polarimeter.

A diode laser (LD852-SEV600), packaged in a tin-oxide (TO) can and tuned to the F=3 to F' transition (852 nm Cs D_2 line) is used to optically pump the atoms and create a strong polarisation. Both vapour cells used in this work contain N_2 buffer gas which decreases the wall collision rate and improves atomic coherence times. As a result of the N_2 content the optical transition lines are collisionally broadened. An optical isolator is placed immediately after the lasers output to prevent unwanted feedback from reflections back to the laser diode. The pump laser power can be adjusted via a combination of waveplates and polarising beam splitters (PBSs). A fraction of the light is directed towards a wavemeter (MOGLABS) for monitoring and control of the lasers frequency. The wavemeter has a PID functionality to ensure that the laser frequency is kept constant. An acousto-optic modulator (AOM) is used to deflect the pump beam into the first order. This is the path the beam follows during the optical pumping stage. During the period when the pump is off the beam remains undeviated in the zeroth order where it is deposited into a beam dump.

For probing of the spin polarised atoms, a DBR laser (DBR895PN) detuned from the collisionally broadened F= 4 – F' transition (895 nm Cs D_1 line) is used. A separate AOM is used for the probe beam in a similar fashion to that of the pump beam. This provides the option of intensity stabilising the optical probe power delivered to the experiment or switching the probe light on (when the pump light is off) or off (when the pump light is on). For the data presented in this work the probe light was always kept on, meaning that intensity stabilisation using the AOM and polarising optics with a pick off of the light to a photodetector and PID servo system (SRS). Both AOMs are driven from the same RF and DC voltage source, ensuring a straightforward synchronisation between the pump and probe periods of the respective laser sources.

The separate laser beams are directed towards a customised multi-wavelength waveplate which is adjusted to ensure that the 852 nm pump light is circularly polarised ($\lambda/4$) and the 895 nm probe light is linearly polarised ($\lambda/2$). The beams then pass through the shield, overlapping at the cell. A band-pass filter reflects the pump light and allows the probe light to be directed towards the polarimeter for detection of the FID signals. This is achieved using a balanced polarimeter where a differential measurement suppresses common mode noise. As a result, this detection system can be more sensitive than using absorption-based detection. The polarimeter, which is connected to a data acquisition device (Picoscope model 5444D) detects rotation of the polarisation plane of the transmitted probe light which is a result of the induced macroscopic magnetisation vector precessing transversely to the orientation of the static field $\vec{B}$. This in turn alters the birefringence of the sample resulting in the two orthogonal circular components of the linearly polarised probe beam enduring different refractive indices. The optical rotation occurring in the perpendicular planes (y and z) to the direction of beam propagation (x) causes a disparity in the projection between these components leading to a constant phase difference of π between them. Subtracting one of these signals from the other is the essence of the differential measurement which produces a greater signal amplitude and lower noise. The separate polarisation states of light are directed to two separate PDs via the use of a HWP and WP combination. The balanced polarimeter subtracts these signals and then amplifies them to give the differential signal. Figure 3 illustrates these orthogonal polarisation states of light with the phase opposition between them highlighted. The figure also displays the differential signal with a noticeable reduction in noise.
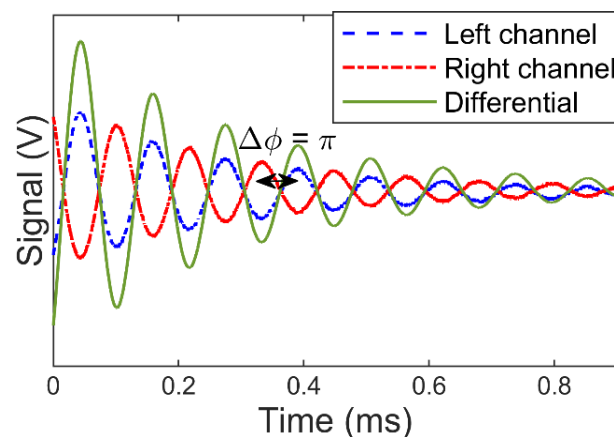

Figure 3: Experimental FID data displaying typical signals. The two orthogonal polarisation states of light (blue trace for left arm of PD and red trace for right arm of PD) are each directed to a separate arm of a balanced polarimeter via a HWP and WP combination. The π phase difference allows a differential measurement (green trace) to be made leading to signal enhancement. All the data shown is experimentally obtained, however, for a clearer illustration the orthogonal polarisation states have been amplified by a factor of 27.5. After subtraction of one of the orthogonal light states from the other this amplification is performed by the polarimeter to give the differential signal.

4.0   RESULTS

4.1   Improved Signals

Figure 4(a) displays an image of a 1.5 mm Cs MEMS cell fabricated at Texas Instruments and a 3 mm cell fabricated at Kelvin Nanotechnology. Figure 4(b) displays one individual FID probe cycle after employing synchronous AM during optical pumping at a bias magnetic field strength of 50 µT to emulate the Earth's magnetic field. The signals were obtained experimentally and subsequently fit to a damped sinusoid model in

post processing. The repetition rate of the sensor which corresponds to the driving frequency of each full pump and probe cycle was set to 1 kHz. 1000 consecutive FID cycles were captured over a total time of 1s; therefore, each combined pump and probe cycle lasts for 1 ms. In both cases the pump laser was tuned to the collisionally broadened F = 3 to F' transition and the probe laser was blue detuned (tens of GHz) to the hybridised F = 4 to F' Cs D_1 line. It is clear from the figure that the greater cell size, and most importantly cell thickness, leads to an improvement in the FID signal amplitude. Additionally, the atomic coherence time is greater in the 3 mm cell primarily due to a lower wall collision rate as a result of the increased thickness and optical path length. The measured mean values for signal amplitude and decay rate were A = 1.64V and γ_2 = 1.7 kHz for the 1.5 mm cell and A = 7.0 V and γ_2 = 1.3 kHz for the 3 mm cell. The increased signal amplitude and atomic coherence times (T_2 coherence time: $T_2 = 1/\gamma_2$) highlight the greater optical pumping efficiency and the greater optical rotation generated in the cell with greater thickness.
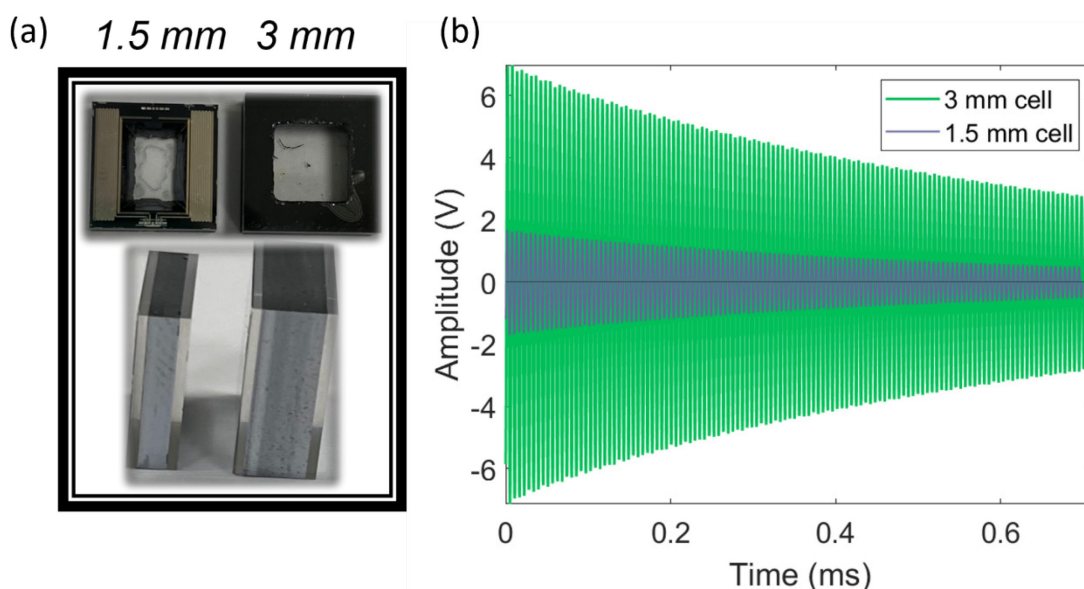

Figure 4: (a) Image of the Cs MEMS vapour cells of two different thicknesses used in this work (b) Single FID cycle for the respective 1.5 and 3 mm cells highlighting the improved signal. Data in both relates to a bias magnetic field strength of 50 µT (oscillation frequency = 175 kHz) after synchronous AM of the optical pumping light.

4.2   Sensitivity Performance

Figure 5 displays the magnetic sensitivity results via a root spectral density plot from the synchronous AM approach carried out as described in the previous section. It should be noted that for the 1.5 mm cell only one sensitivity scan was carried out (one second measurement), whereas the data for the 3 mm cell relates to an average of 40 successive one second measurements. This is purely due to an improved data acquisition capturing approach taken throughout this work. Overall, the improved signals generated in the 3 mm thick cell ultimately leads to an improvement in the magnetic sensitivity. The sensitivity of the 1.5 mm thick cell is around 2.5 pT/$\sqrt{\text{Hz}}$ whereas the sensitivity of the 3 mm cell is around 0.3 pT/$\sqrt{\text{Hz}}$. The quoted sensitivity relates to the region outside of known magnetic noise i.e. 50 Hz noise and harmonics and also a source of magnetic noise separately identified around the 27 to 53 Hz band, which is evident from the 3 mm cell data. Improved shielding and undertaking these measurements in a different laboratory source would likely reduce and mitigate the magnetic noise in this band.
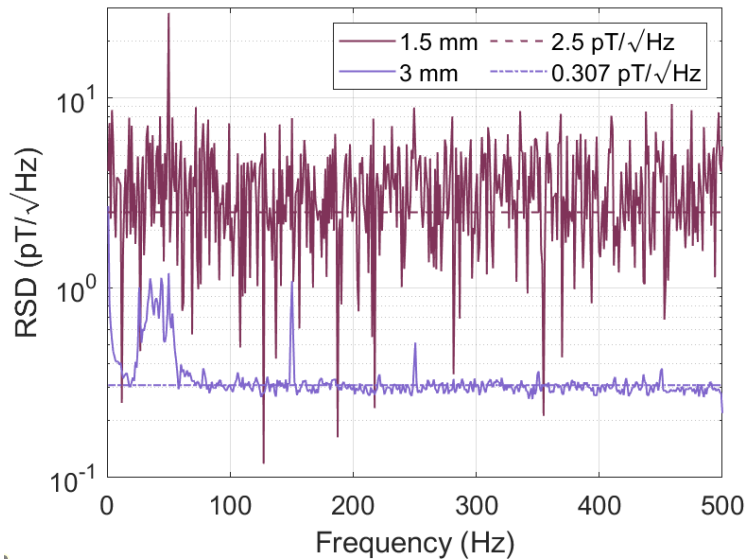
Figure 5: Experimentally obtained magnetic sensitivity results for the 1.5 and 3 mm MEMS cells obtained relating to the signals in section 4.1 in a bias field of 50 µT. The repetition rate of the pump and probe cycles is 1000 Hz leading to a Nyquist limited bandwidth of 500 Hz. The respective dashed line (maroon) and dashed dotted line (blue) are purely a guide to indicate the noise floor for each dataset.

5.0 CONCLUSIONS

Sensitivities in the single pT/$\sqrt{\text{Hz}}$ levels and into the fT/$\sqrt{\text{Hz}}$ levels have been successfully demonstrated through FID magnetometry of 1.5 and 3 mm thick Cs MEMS cells using separate pump and probe lasers. For these respective cell thicknesses magnetic sensitivities of 2.5 pT/$\sqrt{\text{Hz}}$ and 0.3 pT/$\sqrt{\text{Hz}}$ have been accomplished. This has been achieved in a bias magnetic field strength of 50 µT. The bandwidth of the sensor in both cases is 500 Hz (Nyquist limited), however, this can be tailored to suit by adjusting the repetition rate of the sensor as required for any signals of interest at specific frequencies in real-world applications.

An important step in achieving the best possible sensitivity for a given cell is from careful spin-polarisation of the Cs atoms. Ideally the pump laser light should be tuned to a laser frequency as close to the centre of the merged Cs F = 3 to F' transition line. Employing the optimal pumping parameters, particularly with laser frequency, is vital in suppressing the spin exchange collisions that decohere the atoms. Minimising this by tuning to the most appropriate frequencies is extremely beneficial in terms of obtaining signals with high SNRs, coherence times and sensitivities. Utilising cells with larger areas have also proved to be beneficial as there has also be an optimisation through expanding the laser beam diameters for better results. Illuminating the full volume of the cell whilst preserving a high intensity with the pump light increases the SNR. The pump beam intensities and beam diameters can be adjusted in future tests of different MEMS cells with different thicknesses, geometries, and nitrogen buffer gas contents. Optically pumping with enough pump light to saturate the signal amplitudes (on order of > 50 mW) induces a higher degree of polarisation in the sample and leads to signal enhancement.

Overall, an FID sensor is an excellent candidate for future portable or unshielded magnetic sensing applications including defence, mineral exploration and for medical applications i.e. MCG and MEG studies [4], [5]. Exploiting the MEMS cell fabrication facilities at University of Strathclyde where thicker cells with optimised buffer gas pressures will also lead to greater SNRs and sensitivities.

6.0 REFERENCES

[1] J. Fassbinder, Magnetometry for Archaeology, pp. 499–514. 10 2016.

[2] M. Nabighian, et. Al, "75th anniversary - historical development of the gravity method in exploration," Geophysics, vol. 70, 11 2005.

[3] S. Billings et. al, "Magnetic models of unexploded ordnance," IEEE Transactions on Geoscience and Remote Sensing, vol. 44, no. 8, pp. 2115–2124, 2006.

[4] H. Koch, "Recent advances in magnetocardiography," Journal of Electrocardiology, vol. 37, pp. 117 – 122, 2004.

[5] T. M. Tierney et. al, "Optically pumped magnetometers: From quantum origins to multi-channel magnetoencephalography," NeuroImage, vol. 199, pp. 598–608, 2019.

[6] D. Budker and M. Romalis, "Optical magnetome- try," Nature Physics, vol. 3, 12 2006.

[7] H. B. Dang et. al, "Ultrahigh sensitivity magnetic field and magnetization measurements with an atomic magnetometer," Applied Physics Letters, vol. 97, p. 151110, Oct 2010.

[8] D. Hunter et. al, "Free-induction-decay magnetometer based on a microfabricated cs vapor cell," Phys. Rev. Applied, vol. 10, p. 014002, Jul 2018.

[9] S. J. Ingleby et. al, "Vector magnetometry exploiting phase-geometry effects in a double-resonance alignment magnetometer," Physical Review Applied, vol. 10, Sep 2018.

[10] Z. Grujíc et. al, "A sensitive and accurate atomic magnetometer based on free spin precession," The European Physical Journal D, vol. 69, 05 2015.

[11] M. Limes et. Al, "Portable magnetometry for detection of biomagnetism in ambient environments," Phys. Rev. Applied, vol. 14, p. 011002, Jul 2020.

[12] V. Lucivero, et. Al, "Femtotesla direct magnetic gradiometer using a single multipass cell," Phys. Rev. Applied, vol. 15, p. 014004, Jan 2021.

[13] V. Gerginov et. al, "Scalar magnetometry below 100 ft/hz1/2 in a microfabricated cell," IEEE Sensors Journal, vol. PP, pp. 1–1, 06 2020.

[14] J. R. Zimmerman and D. Williams, "Nuclear gyromagnetic ratios of be9, rb85, rb87, and cs133," Phys. Rev., vol. 75, pp. 699–699, Feb 1949.

[15] M. P. Ledbetter et. al, "Zero-field remote detection of nmr with a microfabricated atomic magnetometer," Proceedings of the National Academy of Sciences, vol. 105, no. 7, pp. 2286–2290, 2008.

[16] V. Tiporlini and K. Alameh, "High sensitivity optically pumped quantum magnetometer," TheScientificWorldJournal, vol. 2013, p. 858379, 05 2013.

[17] R. Jiménez et. Al, "High-bandwidth optical magnetometer," J. Opt. Soc. Am. B, vol. 29, pp. 3398–3403, Dec 2012.

[18] T. Scholtes et al, Phys. Rev. Applied vol 84, 043416, (2012).